nature materials

SUPPLEMENTARY INFORMATION

DOI: 10.1038/NMAT4842

In the format provided by the authors and unedited.

Three-dimensional imaging of dislocation dynamics during the hydriding phase transformation

A. Ulvestad[1]*, M. J. Welland[2], W. Cha[1], Y. Liu[1], J. W. Kim[3], R. Harder[3], E. Maxey[3], J. N. Clark[4], M. J. Highland[1], H. You[1], P. Zapol[1], S. O. Hruszkewycz[1], and G. B. Stephenson[1]

[1]Materials Science Division, Argonne National Laboratory, Argonne, Illinois 60439, USA

[2]Fuel & Fuel Channel Safety Branch, Canadian Nuclear Laboratories, Chalk River, Ontario K0J 1J0, Canada

[3]Advanced Photon Source, Argonne National Laboratory, Argonne, Illinois 60439, USA

[4]Stanford PULSE Institute, SLAC National Accelerator Laboratory Menlo Park, California 94025, USA

*aulvestad@anl.gov

Supporting Information

Single Particle Coherent Diffraction Data. Supplementary Fig. 3 shows the central cross section from 3D coherent diffraction data sets collected about the 111 diffraction peak for the same particle as a function of p_{H2} exposure time. The diffracted intensity patterns evolve significantly as a function of exposure time. The initial pattern is nearly centrosymmetric, indicating that the Pd nanoparticle was minimally strained[1]. The diffraction pattern also shows well-defined fringes, which are generated by the sharp facets of the nanocrystal. Significant changes in the diffracted intensity pattern are seen after 30 minutes of p_{H2} exposure. Some fringes remain, indicating the presence of sharp facets in the nanocrystal, while most fringes became less pronounced. By 247 minutes of p_{H2} exposure, the peak has broadened and become more diffuse. We found that the α phase (111) peak persists in the area detector (Supplementary Fig. 11), indicating that

the crystal has not completely transformed to the β phase. The β phase 111 Bragg condition is sufficiently different from the α phase 111 Bragg condition that, in contrast to the ensemble measurements discussed in Fig. 4, β phase diffraction does not appear on the area detector in the BCDI measurements. The reversibility of the hydriding transformation was explored by exposing the particle to pure He (p_{H2} = 0) at room temperature and at 50 C for over one hour. We found that the diffraction intensity distribution never returns to its original state (Supplementary Fig. 12), indicating that nanoparticle changes induced by hydrogen exposure were irreversible.

Phase field governing equations.

Assuming instantaneous elastic relaxation relative to diffusion, the displacement vector u_i is solved for quasi-statically within a virtual work formulation:

$$0 = \int_V \sigma_{ij}\delta\epsilon_{ij}\, dV + \int_A \left\{f^S\delta\epsilon_{ii}^S + \sigma_{ij}^S\delta\epsilon_{ij}^S\right\}dA \qquad (4)$$

where the virtual strain $\delta\epsilon_{ij}$ has been projected onto the surface as described before.

The chemical potential of interstitial hydrogen defined as

$$\mu = \frac{1}{\rho}\frac{\delta F}{\delta x} = \frac{1}{\rho[x^\beta - x^\alpha]}\frac{\delta F}{\delta p} \quad ,$$

gives the governing equations for the volume and surface:

$$\mu = \frac{1}{\rho[x^\beta - x^\alpha]}\left[\frac{\partial f + \frac{1}{2}\sigma_{ij}\epsilon_{ij}^{el}}{\partial p} - \kappa\nabla^2 p\right] \quad on \quad V, \; \frac{1}{\rho[x^\beta - x^\alpha]}\left[\frac{\partial \frac{1}{2}\sigma_{ij}^S\epsilon_{i\square}^{el,S}}{\partial p} + n_i \cdot \kappa\nabla p\right] \quad on\, A \quad (5)$$

Currently, only the steady state, equilibrium situation is considered to describe strain distributions for different average *x*. However, the time-dependent case is solved for the sake of numerical robustness. The concentration of H evolves according to a Langevin type equation:

$$\rho\frac{\partial x}{\partial t} = \nabla \cdot \rho\frac{x[1-x]D}{RT}\nabla\mu \quad (6)$$

where the diffusion coefficient, *D*, is set to unity as it does not affect the equilibrium

distribution. Equations 4-6 are solved for variables u_i, μ and x using the finite element method implemented in the FEniCS package[2–5]. The mesh was locally refined to achieve a mesh size of less than 1.5 nm at the interface. Problems reached 4 million degrees of freedom, and were solved using up to 512 cores on a high-performance Linux cluster at Argonne National Laboratory. Initial conditions were microstructures similar to the anticipated steady state, which helped minimize pseudo-time steps and computational expense. While the initially cap microstructures remained so, the core-shell microstructures immediately began to collapse. Calculations of elastic energy in core-shell particles were therefore made without diffusion of H.

Variable Pressure Ensemble Diffraction Experiment Details. Ensemble experiments were performed at Sector 12-ID-D of the Advanced Photon Source at Argonne National Laboratory. A double crystal monochromator was used to select E=24 keV x-rays. Slits were used to reduce the beamsize to approximately $5\times30\ \mu m^2$ (vertical x horizontal) for the measurement discussed in Supplementary Figure 15. The Pd (111) Bragg peak was collected using a 2D area detector (Pilatus, each pixel 172μm x 172μm) placed at a scattering angle of 13° and at a distance of 0.845 m from the sample. Each 2D diffraction pattern used a 2 second exposure time. Measurements were performed at room temperature (300 K) at a total pressure of 26664 Pa. The nitrogen gas was then progressively diluted with hydrogen gas to increase the hydrogen partial pressure. Figure S14a shows the Pd (111) Debye-Scherrer ring (a ring of fixed scattering angle, 2Θ) from the as-prepared state. The initial ring shows significant intensity variation with bright spots resulting from individual crystalline particles. Figure S14b shows the diffraction intensity distribution at t=50 minutes. The presence of two rings in the intensity pattern indicates bulk two-phase coexistence under these conditions. A single β phase ring (Figure S14c) exists at 9332 Pa p_{H2}. After the full transformation, we note that the

intensity distribution along the ring is much more uniform, lacking the bright spots of the as-prepared state. This change in the intensity distribution can be attributed to dislocation generation[6]. We then decreased p_{H2} to dehydride the particles. Figure S14d shows that two-phase coexistence persists during dehydriding down to 266 Pa, indicating a hysteresis between the hydriding and dehydriding two-phase coexistence pressures, as previously observed[7,8]. Figure S14e shows the intensity distribution along the ring after complete dehydriding, which is more uniform than Fig. S14a. Figure S14f shows the integrated intensity as a function of hydrogen partial pressure.

Supporting Figures.

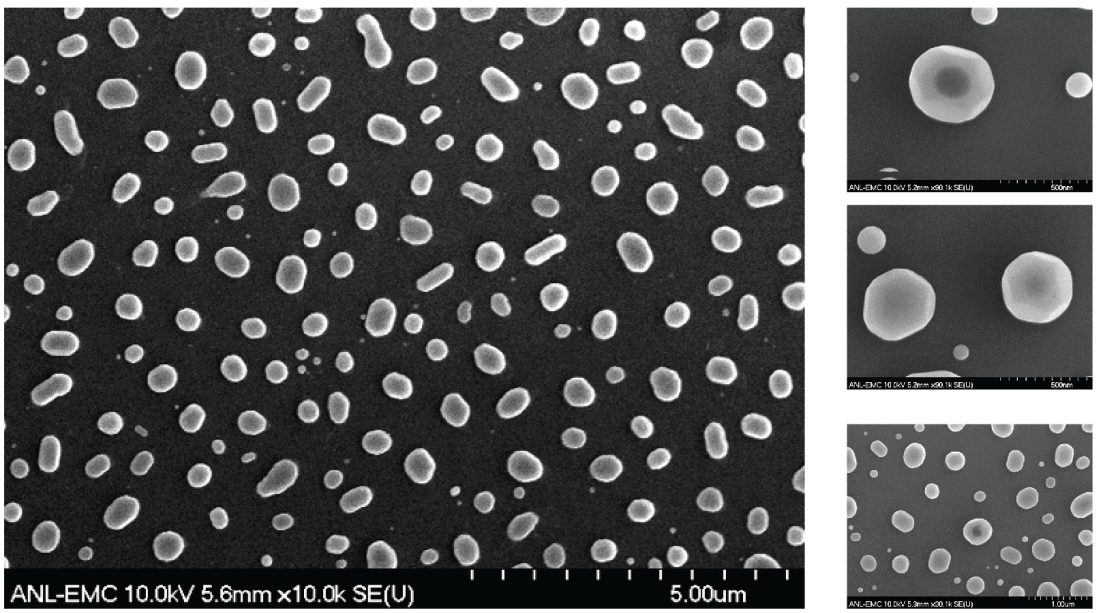

Figure S1. SEM images of Pd nanoparticles formed by the dewetting procedure.

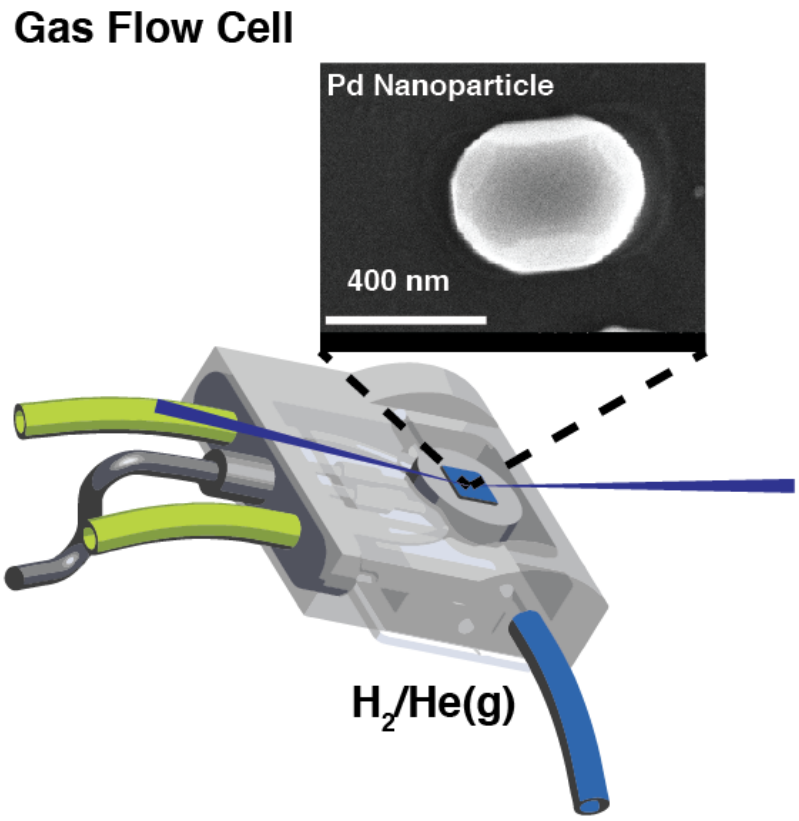

Figure S2. Gas environmental cell schematic and electron microscopy image of a Pd nanoparticle.

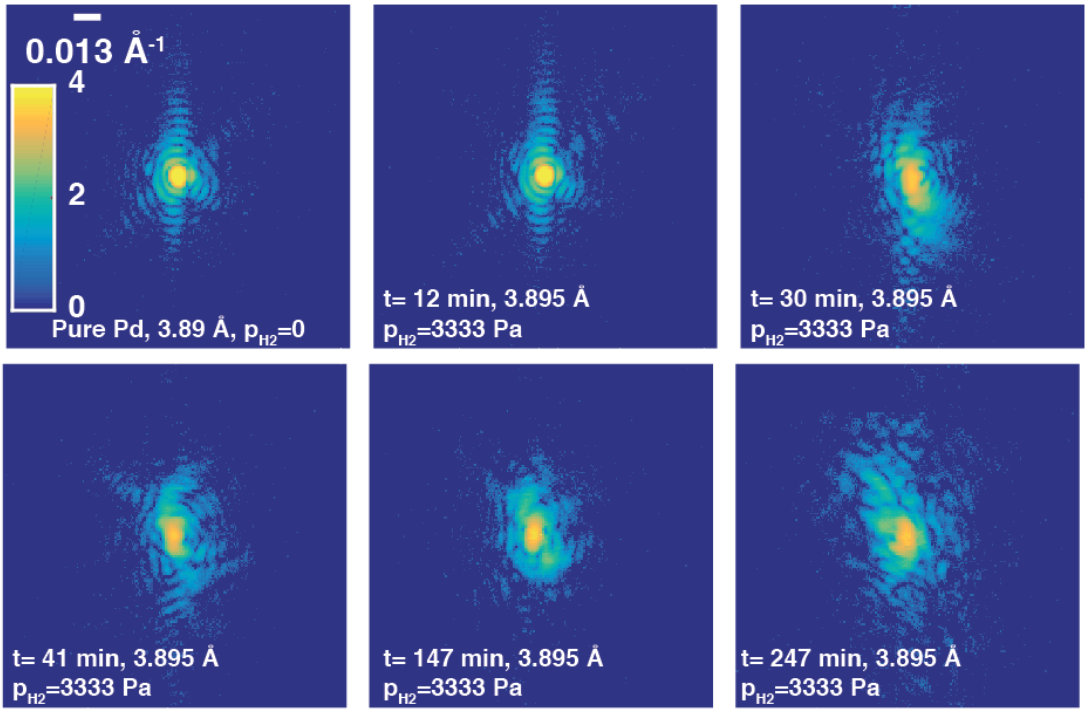

Figure S3. Evolution of the central Bragg peak cross-section (from 3D coherent diffraction data sets) for a single Pd nanoparticle as a function of exposure time. Colorbar and scalebar apply to all images. Colorbar is the $\log_{10}$ of the number of photons. 3D measurements were collected at each time state. These diffraction data sets correspond to the reconstructions shown in Figure 2.

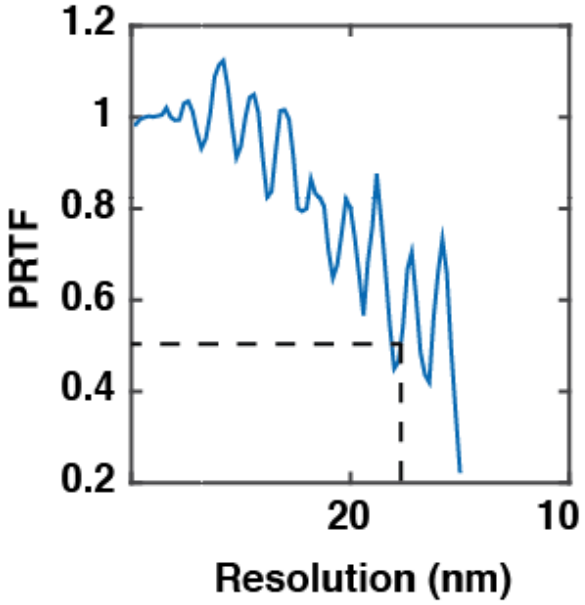

Figure 4 Phase retrieval transfer function. A cutoff of 0.5 is applied to determine the spatial resolution of approximately 18 nm.

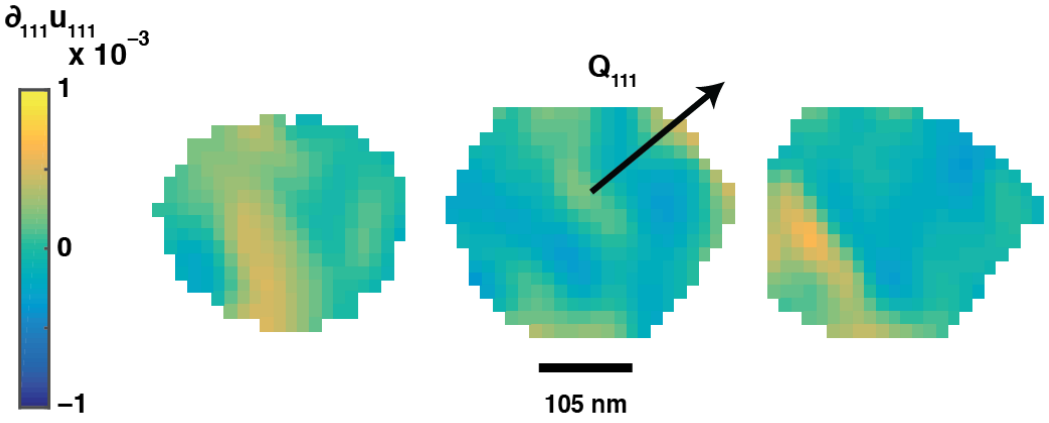

Figure S5. Baseline compressive/tensile strain at the four cross-sections. Maximal strains are on the order of 5x10^{-4}. Black vector shows the (111) scattering vector.

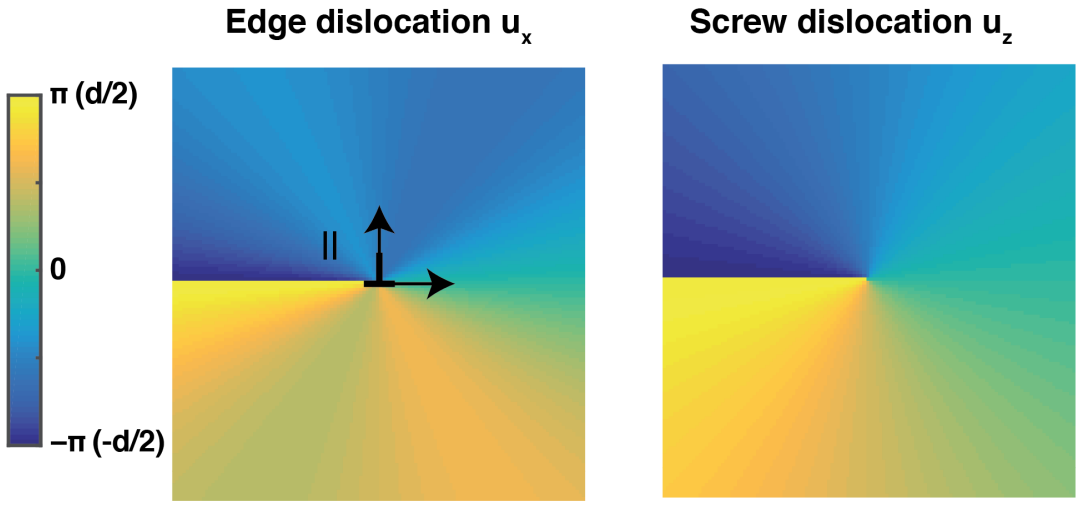

Figure S6. Displacement field components for an edge and screw dislocation. The magnitude of the u_x displacement field component for the edge dislocation is shown, while the magnitude of the u_z displacement field component is shown for the screw dislocation. d is the crystal lattice parameter.

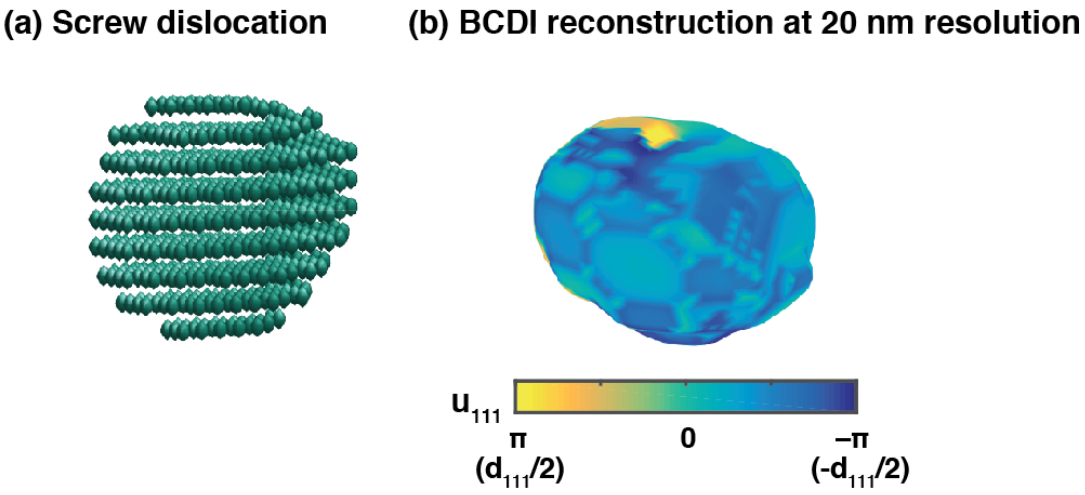

Figure S7. The effect of BCDI resolution on the ability to resolve dislocations. a, the screw dislocation model made up of atoms. b, the BCDI reconstruction at 20 nm resolution. The atoms are blurred out but the dislocation is visible in the displacement field, which is projected onto the isosurface.

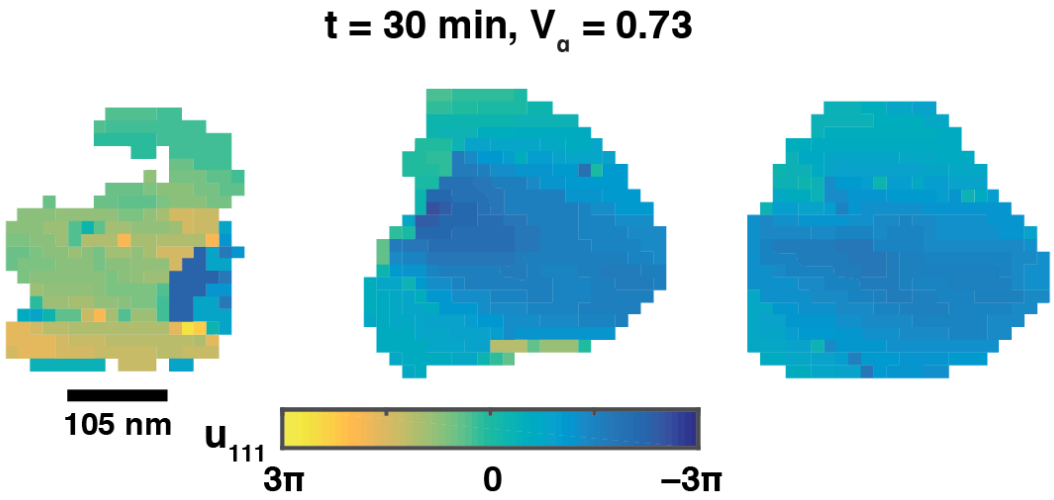

Figure S8. The unwrapped phases for a state in Fig. 2. The phases were unwrapped using a Goldstein 2D phase unwrapping method.

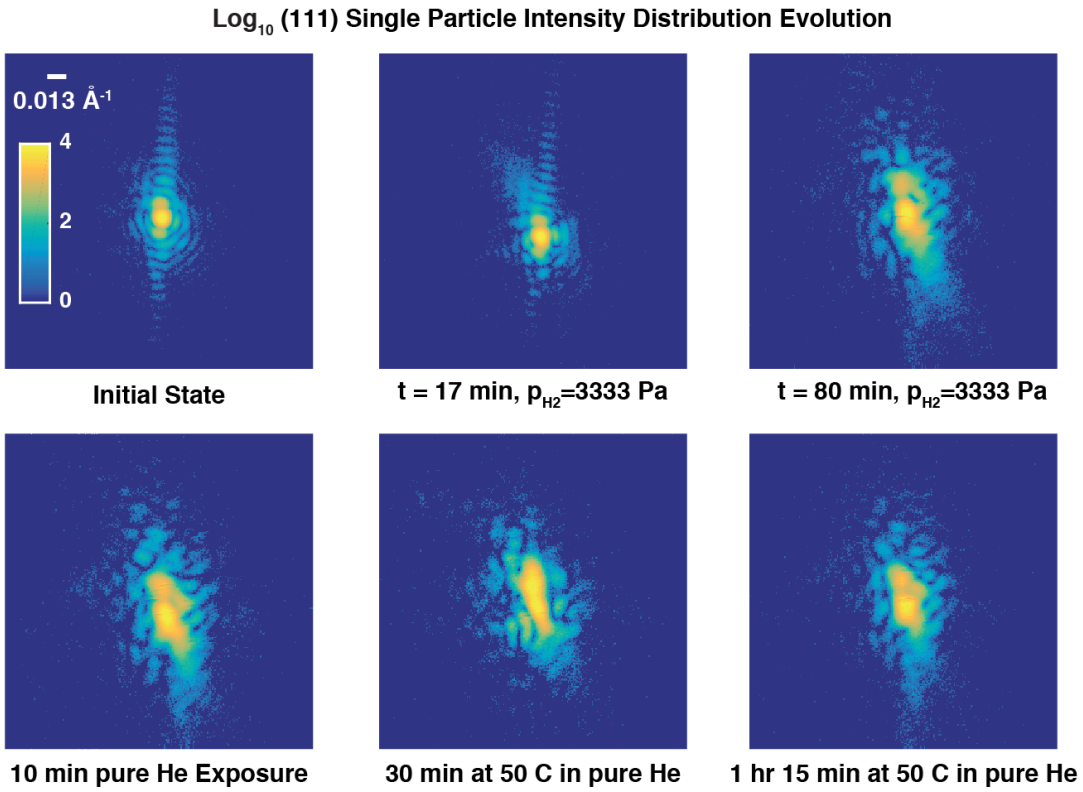

Figure S9. Evolution of the central Bragg peak cross-section (from 3D coherent diffraction data sets) for a different, single Pd nanoparticle as a function of exposure

time. Colorbar and scalebar apply to all images. Colorbar is the $\log_{10}$ of the number of photons. 3D measurements were collected at each time state.

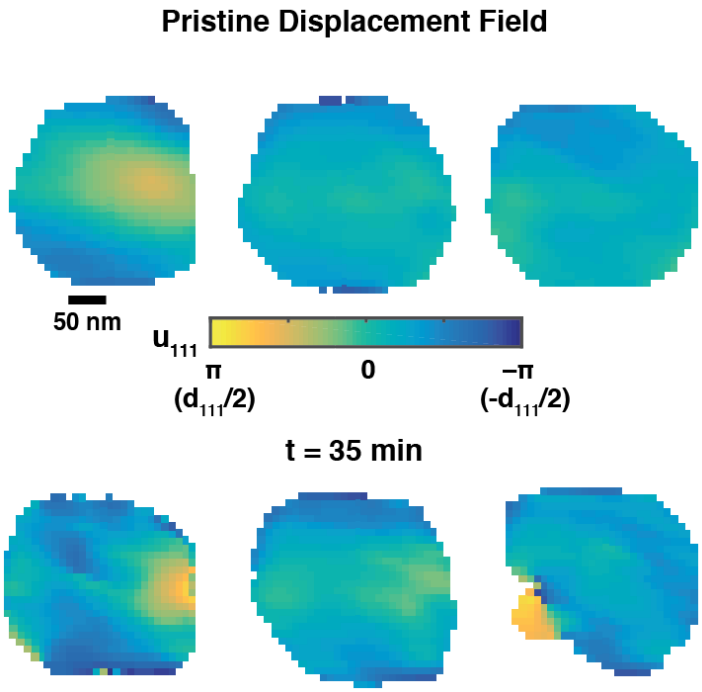

Figure S10. Displacement field ($u_{111}(\mathbf{r})$) maps at 3 cross-sections are shown prior to hydrogen exposure for another single particle. After 35 minutes of hydrogen exposure, part of the particle has transformed and there is a dislocation near the boundary of the remaining α phase.

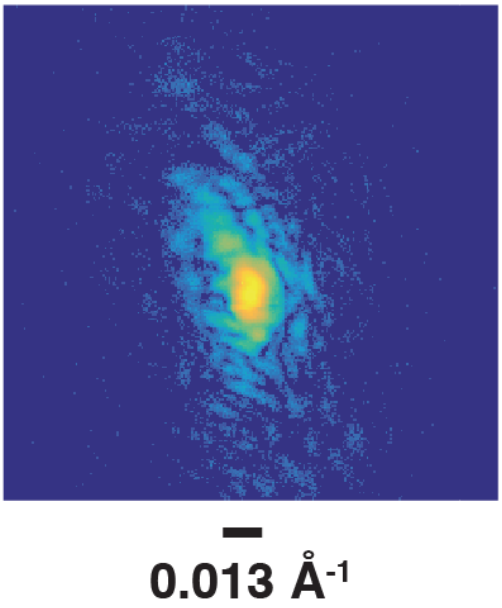

Figure S11. Diffraction cross-section from the single Pd nanoparticle discussed in the text (Fig. 2) after 390 minutes exposure to 3333 Pa p_{H2}.

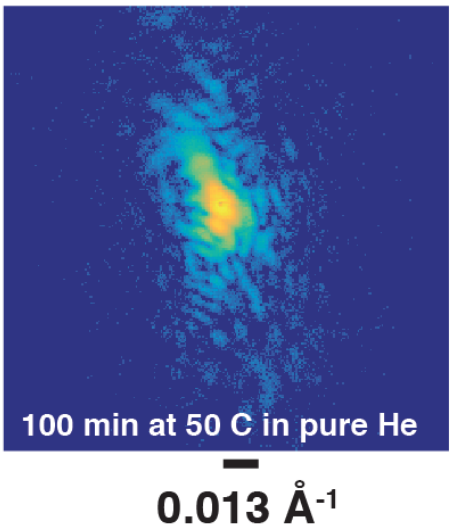

Figure S12. Diffraction cross-section from the single Pd nanoparticle discussed in the text (Fig. 2) during p_{H2} = 0 Pa. A pure He flow was first used, followed by He flow at elevated temperature (50 C). The changes induced during the hydriding phase transformation are not reversed by these conditions.

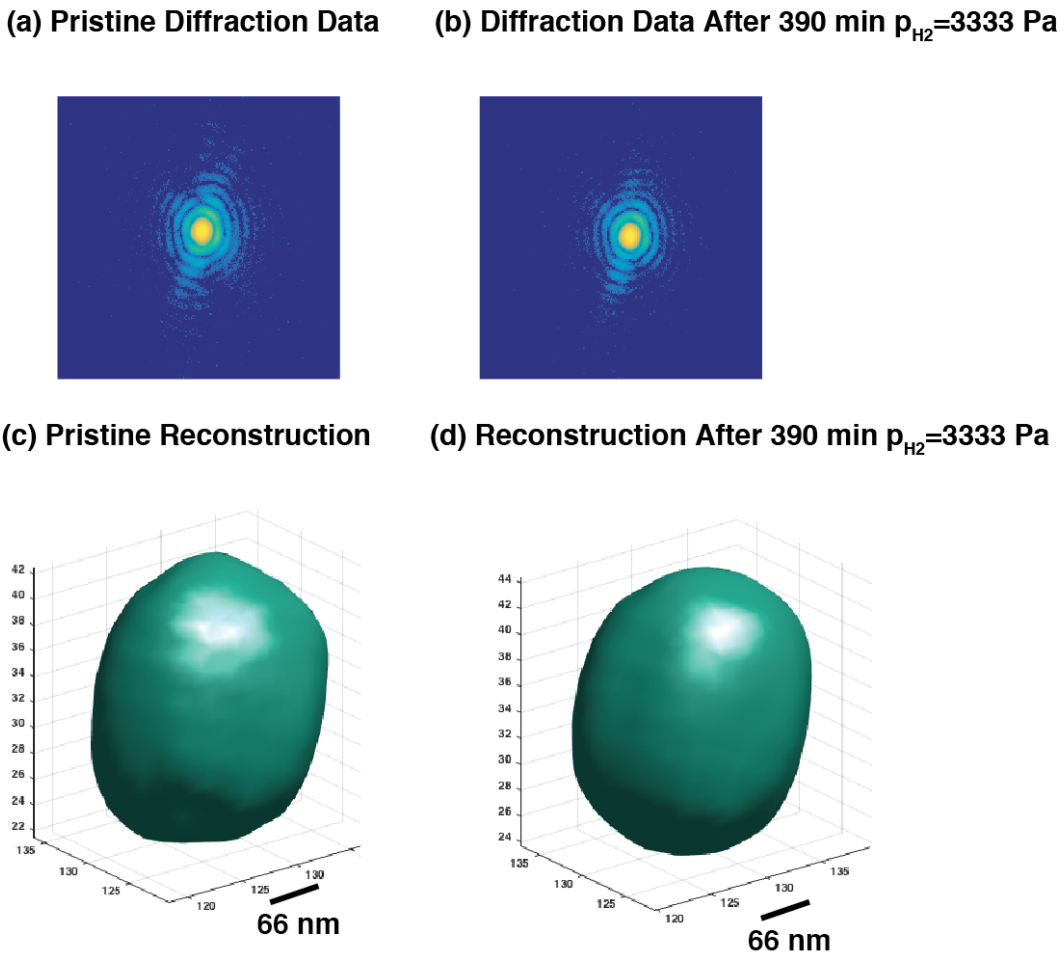

Figure S13. No changes observed in a different particle during hydrogen exposure. **a**, the central cross-section of the initial diffraction data. **b**, the central cross-section of the diffraction data after 390 minutes of exposure to 3333 Pa p_{H2}. **c**, the real space reconstruction of the particle. Axes are in pixels and one pixel is approximately 13 nm. The particle is approximately 270x270x135 nm^3, with the smallest dimension normal to the substrate. **d**, the real space particle shape and size after 390 minutes of exposure to 3333 Pa p_{H2}.

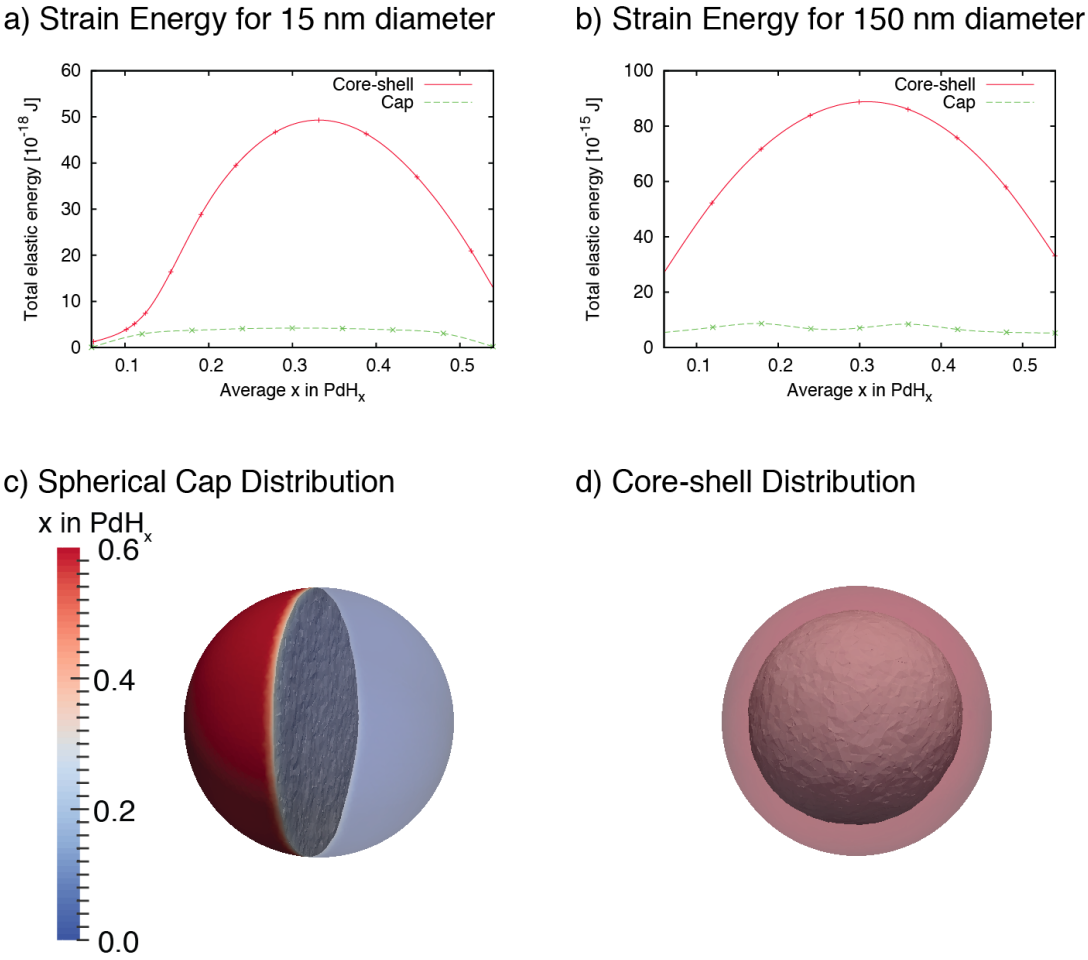

Figure S14. Difference in strain energy for a core/shell vs. spherical cap two-phase distribution for two different spherical particles. x corresponds to the x in PdH_x. **a**, the strain energy for a 15 nm diameter particle. **b**, the strain energy for a 150 nm diameter particle. **c**, an example of a spherical cap distribution. **d**, an example of a core-shell distribution.

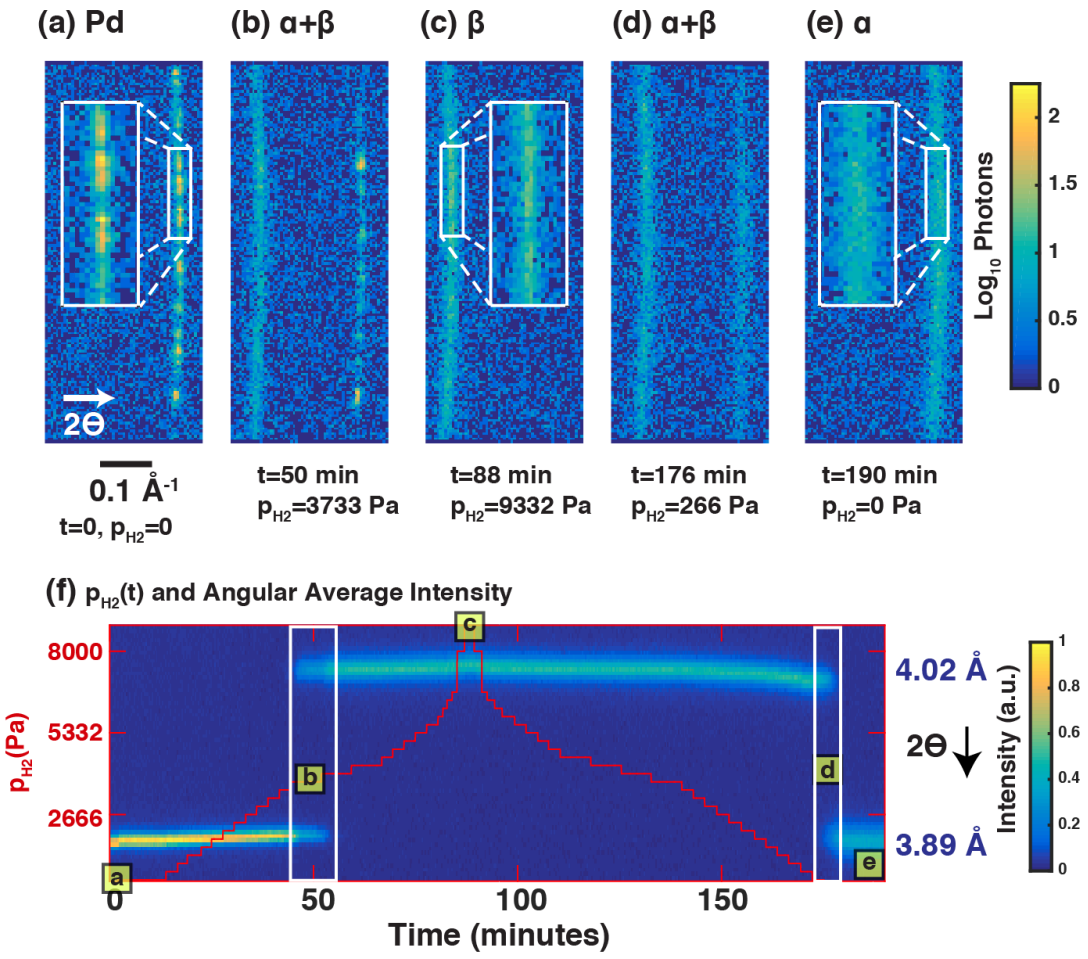

Figure S15. Ensemble Pd behavior during hydrogen partial pressure variation. a, Debye-Scherrer ring from diffraction by the Pd (111) lattice planes from the as-synthesized sample. The white boxes show magnifications of particular regions along the ring; 2Θ is the scattering angle**.** The scalebar applies to 1a-e**. b**, Snapshot of bulk two-phase coexistence observed during the phase transformation. **c**, Snapshot after complete transformation to the lattice expanded β phase. **d**, Snapshot of bulk two-phase coexistence observed during the dehydriding transformation. **e**, Snapshot after complete transformation to the α phase. **f**, angularly averaged intensity as a function of hydrogen pressure.

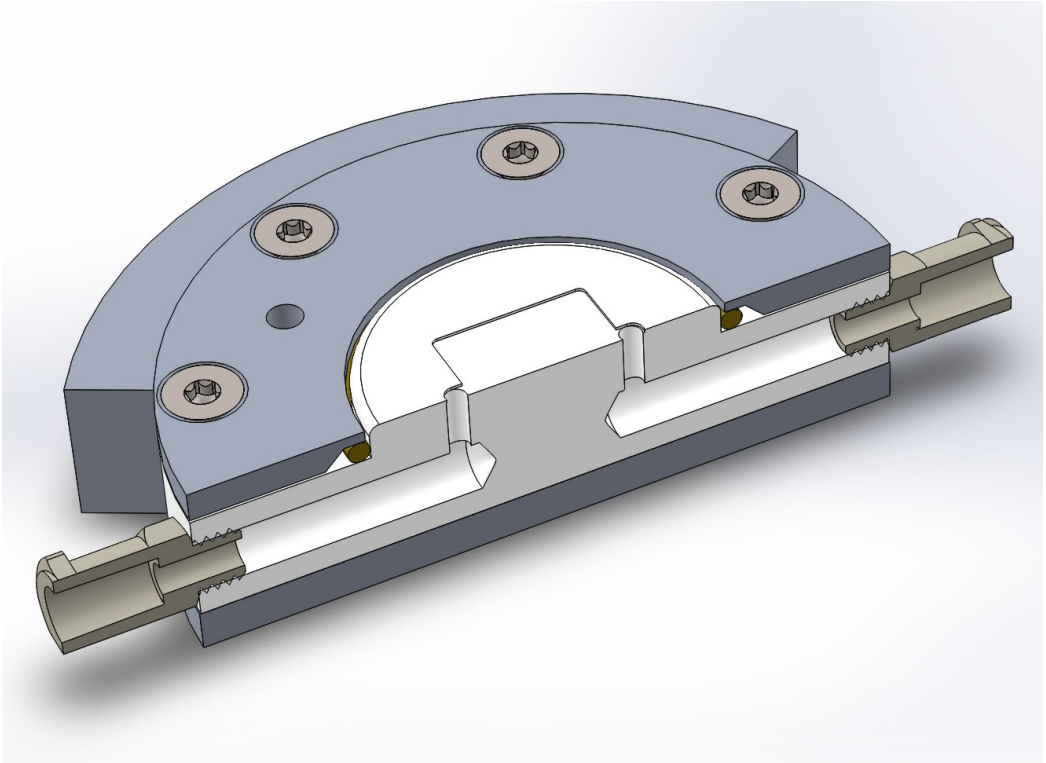

Figure S16. Cutaway view of the in-situ environmental x-ray gas cell used for the variable pressure experiments. A Mylar film allows x-rays to enter and exit the environment while maintaining pressure in the cell.

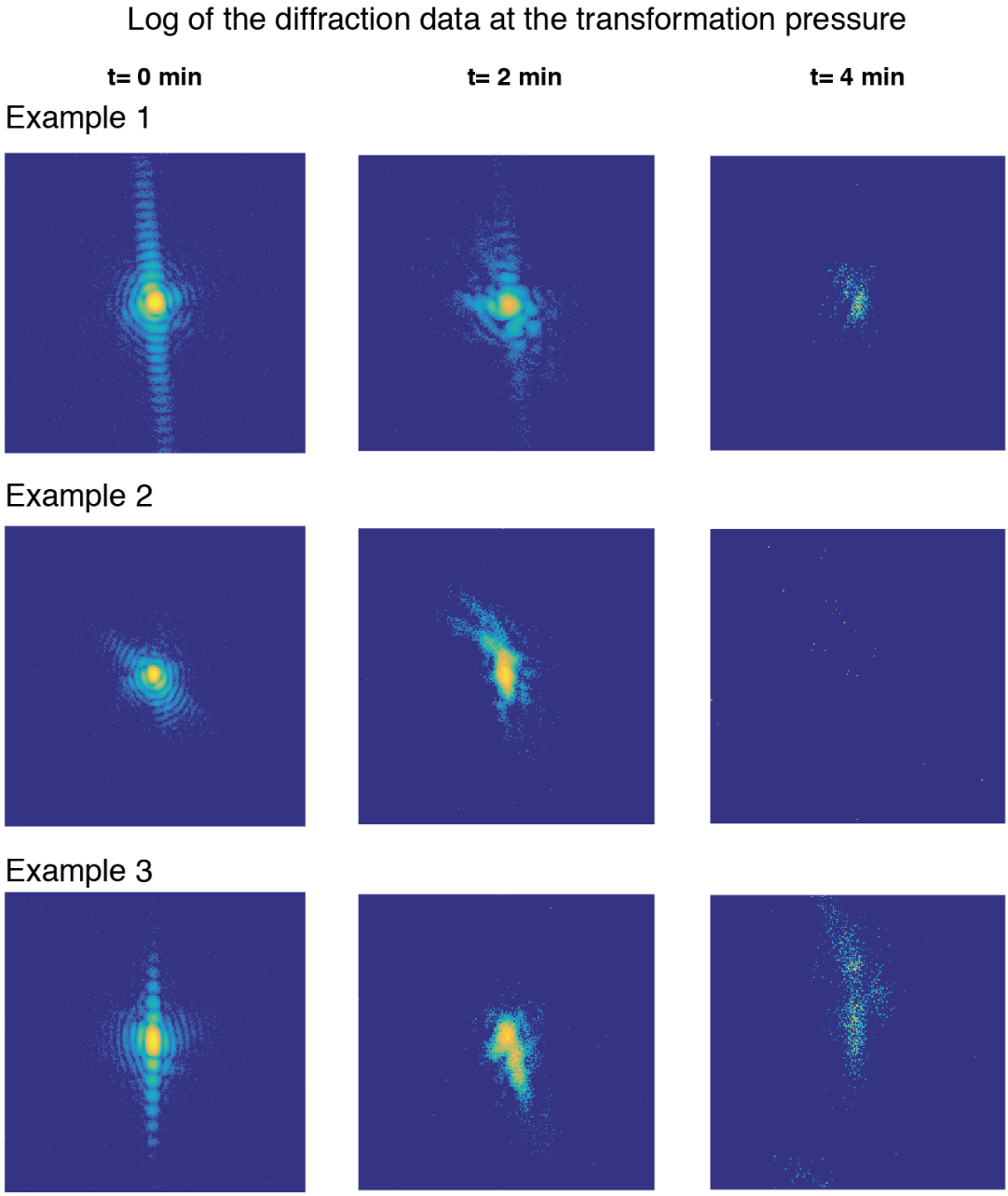

Figure S17. Diffraction data changes for three particles at the transformation pressure. At the transformation pressure in Fig. 5, the α phase diffraction typically disappears in 3-6 minutes. The log of the diffraction data is shown and all images are rescaled to show the changes more clearly.

References:

1. Robinson, I. & Harder, R. Coherent X-ray diffraction imaging of strain at the nanoscale. *Nat. Mater.* **8,** 291–8 (2009).
2. Logg, A., Olgaard, K. B., Rognes, M. E. & Wells, G. N. in *Automated Solution of Differential Equations by the Finite Element Method, Volume 84 of Lecture Notes in Computational Science and Engineering* (eds. Logg, A., Mardal, K.-A. & Wells, G. N.) (Springer, 2012).
3. Logg, A. & Wells, G. N. DOLFIN: Automated Finite Element Computing. *ACM Trans. Math. Softw.* **37,** (2010).
4. Kirby, R. C. & Logg, A. A Compiler for Variational Forms. *ACM Trans. Math. Softw.* **32,** (2006).
5. Alnæs, M. S., Logg, A. & Mardal, K.-A. in *Automated Solution of Differential Equations by the Finite Element Method, Volume 84 of Lecture Notes in Computational Science and Engineering* (eds. Logg, A., Mardal, K.-A. & Wells, G. N.) (Springer, 2011).
6. Jamieson, H. C., Weatherly, G. C. & Manchester, F. D. The β → α phase transformation in palladium-hydrogen alloys. *J. Less Common Met.* **50,** 85–102 (1976).
7. Flanagan, T. B. & Oates, W. A. THE PALLADIUM-HYDROGEN SYSTEM. *Annu. Rev. Mater. Res.* **21,** 269–304 (1991).
8. Manchester, F. D., San-Martin, A. & Pitre, J. M. The H-Pd (hydrogen-palladium) System. *J. Phase Equilibria* **15,** 62–83 (1994).